

THESIS

**A Study of Baseline Compensation
System for Stable Operation of
Gravitational-wave Telescope**

Koseki Miyo

*Department of Physics
University of Tokyo*

MMM 2020

Contents

Chapter 1

Background

1.1 Gravitational-wave

1.1.1 ...

1.2 Sources of Gravitational-wave

1.2.1 ...

1.3 Interferometric Gravitational-wave detection

1.3.1 Detection Principle

地上の大型重力波検出器の基本要素は Michelson 型レーザー干渉計である。プラスモードの重力波が Fig.?? に示すような Michelson 型レーザー干渉計を垂直に通過する場合を考える。

1.3.2 Michelson Interferometer

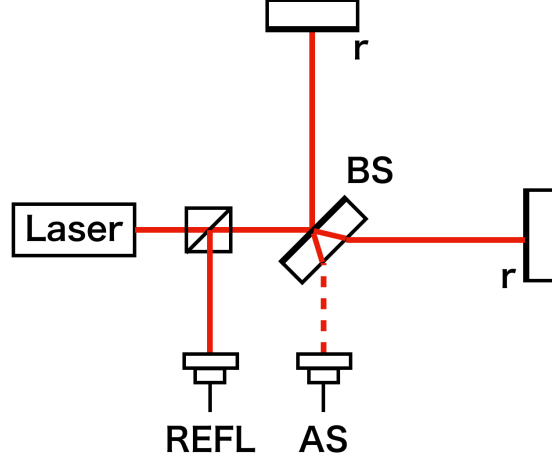


Figure 1.1: Michelson Interferometer.

Michelson interferometer is a converter from the optical phase difference of two lights to the amplitude modulation of a single light. Consider about the interferometer shown in Fig. 1.1. Incident light can be written as,

$$E_{\text{in}} = E_0 e^{i\omega t}, \quad (1.1)$$

where E_0 is the amplitude and ω_0 is the angular frequency of the laser field. Two lights split by the Beam Splitter (BS) interfere at the Anti-symmetric (AS) port and Reflection (REFL) port. The output field at the AS port is represented as,

$$E_{\text{AS}} = -\frac{1}{2}rE_0 e^{i(\omega_0 t - \phi_x)} + \frac{1}{2}rE_0 e^{i(\omega_0 t - \phi_y)}, \quad (1.2)$$

where r denotes the amplitude reflectivity of the end mirrors, and ϕ_x and ϕ_y are the phase delay due to the light traveling in the x and y arms. This output signal can be represented as a single field as,

$$E_{\text{AS}} = irE_0 e^{i(\omega_0 t - (\phi_x + \phi_y)/2)} \sin\left(\frac{\phi_x - \phi_y}{2}\right). \quad (1.3)$$

We find that the amplitude of the output light is a function of the difference between two phases; $\phi_x - \phi_y$. Furthermore, the power of output light at the AS port is obtained by squaring the Eq. 1.3,

$$P_{\text{AS}} = (rE_0)^2 [1 - \cos(\phi_x - \phi_y)] \quad (1.4)$$

Similarly, power of the output light as REFL port is written as,

$$P_{\text{REFL}} = (rE_0)^2 [1 + \cos(\phi_x - \phi_y)]. \quad (1.5)$$

Therefore, we can measure the optical phase difference as the amplitude changes using a Photo Detector (PD) and detect GWs.

1.3.3 Null Measurement

Shot Noise

Shot noise is the optical readout noise associated with the discrete nature of photons and electric charges. 光のパワーは

Control Noise

1.4 Summary of the Chapter

Chapter 2

KAGRA

2.1 Overview

2.1.1 ...

2.1.2 ...

2.2 KAGRA Tunnel

2.2.1 Tunnel Design

KAGRA tunnel is excavated in the Kamioka mine in Hida, Gifu, Japan [?]. The tunnel is consisted of two floors. 干渉計を構成するほとんどの鏡は 1 階に設置された防振装置で懸架されているが、腕共振器を構成する 4 つの鏡は 1 階から 14m の高さにある 2 階から懸架されている。

The tunnel is locate under 200 m from ground surface to decrease the seismic noise effectively.

2.2.2 Geological features

Hida region to which Kamioka belongs is a ancient region in Japan island [?].

The main bedrock is the geniss.

2.3 Main Interferometer

2.3.1 Overview

KAGRA is a cryogenic intergerometric gravitational-wave detector constructed at the underground site of Kamioka mine [?].

2.3.2 Main Interferometer

Design

The design of KAGRA interferometer is dual recycled Fabry-Perot Michelson interferometer [?][?].

2.4 Vibration Isolation System

2.4.1 Overview

KAGRA has 4 types vibration isolation system.

2.4.2 Type-A Suspension System

Type-A suspensions are developed [?].

2.5 Summary of the Chapter

Chapter 3

Seismic Noise

Seismic noise causes two issues for laser interferometric gravitational-wave detectors; (1) limitation of the low-frequency sensitivity of the detectors and (2) deterioration of the duty cycle of that. The seismic noise above 1 Hz, which is associated with anthropogenic activity, contaminates the low-frequency sensitivity. The seismic motion below this frequency, which is generated by the natural noise source such as the ocean, disturbs the Fabry-Perot arm cavity to resonate stably.

In order to resolve these issues, a laser interferometer gravitational wave antenna with a baseline length of 20 m (LISM) [?] is constructed underground, because the low-level seismic noise is expected in the underground environment. As a result, the seismic noise in LISM site is less than that in the surface site by two orders of magnitude in 1–100 Hz region, and the underground GW detector performed stable operation with duty cycle of 99.8%.

However, for km-meter scale GW detector like KAGRA, such a stable operation can not be expected because

- length of the long baseline is susceptible to the low-frequency seismic motion compared with the short one due to the a few reduction effect kind of the *common mode rejection*, and this problem is common in not only all the current detectors but also the next 10 km-scale detectors; Einstein Telescope (ET)[?] and Cosmic Explorer (CE) [?].
- especially in KAGRA site, the microseismic noise correlated with the ocean activity in 0.03–0.3 Hz, which is the most problematic noise for stable operation of GW detector, cannot be reduced even in the underground due to near the sea (40 km from Toyama Bay), and this problem is common in ET which is also will be constructed in underground but in island [?].

The purpose of this chapter is to describe quantitatively above two problems. In this chapter, first, section 3.1 gives an theoretical understanding of the seismic

noise as the elastic waves. In section 3.2, some general properties of the seismic noise are described by quoting previous researches. Finally, we discuss the problems in section 3.3.

3.1 Theory of seismic waves

Here we introduce characteristics of the seismic wave that will be useful in our later understanding and modeling of seismic effects.

3.1.1 Seismic Waves

The elastodynamic wave equation without external forces is given by

$$\rho \ddot{\mathbf{u}} = (\lambda + 2\mu) \nabla(\nabla \cdot \mathbf{u}) - \mu \nabla \times (\nabla \times \mathbf{u}), \quad (3.1)$$

where \mathbf{u} is the displacement field vector of the medium, ρ denotes density of the medium, and λ, μ are Lamé's first and second parameter.

Body Waves

From Eq.(3.1), we can obtain two characteristic waves; longitudinal wave (primary wave, P-wave) and transverse wave (secondary wave, S-wave). First, using Helmholtz's decomposition, we represent the displacement field vector \mathbf{u} as

$$\mathbf{u} = \nabla \phi + \nabla \times \boldsymbol{\psi}, \quad (3.2)$$

where ϕ the scalar potential and $\boldsymbol{\psi}$ are the vector potential. Each term of Eq.(3.2) show the divergent and the rotation component of \mathbf{u} respectively. Substitute Eq.(3.2) into Eq.(3.1) and after some vector algebra, one can obtain two wave equations;

$$\ddot{\phi} = v_L^2 \nabla^2 \phi, \quad (3.3)$$

$$\ddot{\boldsymbol{\psi}} = v_T^2 \nabla^2 \boldsymbol{\psi}, \quad (3.4)$$

where v_L, v_T are defined as

$$v_L = \sqrt{\frac{\lambda + 2\mu}{\rho}}, \quad v_T = \sqrt{\frac{\mu}{\rho}}. \quad (3.5)$$

These phase velocities; v_L, v_T represent that of the P-wave and the S-wave. Show this relationships. Because the scalar potential and the vector potential are obey the wave equation Eq.(3.3) and Eq.(3.4) respectively, the general solutions of these potentials are given as

$$\phi = \phi_0(\omega t - \mathbf{k} \cdot \mathbf{x}) \quad (3.6)$$

$$\boldsymbol{\psi} = \boldsymbol{\psi}_0(\omega t - \mathbf{k} \cdot \mathbf{x}), \quad (3.7)$$

where ω , \mathbf{k} are the angular frequency and the wave vector. One can obtain the divergent component of displacement field vector \mathbf{u} as

$$\mathbf{u}_{\text{div}} = \nabla \phi_0(\omega t - \mathbf{k} \cdot \mathbf{x}) = -\mathbf{k} \phi. \quad (3.8)$$

The displacement of this wave \mathbf{u}_{div} whose phase velocity is v_L propagates along with direction of the wave vector. Therefore v_L is the phase velocity of a longitudinal wave called P-wave. On the other hands, one can obtain the rotation component of \mathbf{u} as

$$\mathbf{u}_{\text{rot}} = \nabla \times \psi_0(\omega t - \mathbf{k} \cdot \mathbf{x}) = -\mathbf{k} \times \psi. \quad (3.9)$$

This displacement vector \mathbf{u}_{rot} whose phase velocity is v_T is perpendicular to the wave vector. Therefore, v_T is the phase velocity of a transverse wave called S-wave. Furthermore, because λ and μ are positive numbers,

$$v_L > v_T. \quad (3.10)$$

Therefore, the longitudinal wave is faster than the transverse wave.

Rayleigh waves

Rayleigh wave は P 波と S 波の干渉によって生じる []。ここでは Z 軸を鉛直方向とした直交直線座標系の x-z 面内で振動する弾性波を考える。z=0 を自由表面とし、x 軸に沿って P 波と S 波が同じ速度 $v_R = \omega/k$ (ω is angular frequency and k is the wave vector) で伝搬する場合を考えると、ポテンシャル ϕ と ψ は、それぞれ以下のように表すことができる。

$$\phi = F(z) \exp[i(kx - \omega t)], \quad (3.11)$$

$$\psi = G(z) \exp[i(kx - \omega t)] \quad (3.12)$$

Eq.3.11 と Eq.3.11 を波動方程式 Eq.3.3, Eq.3.4 に代入すれば、レイリー波の特性方程式が導かれる;

$$\left(\frac{c_R^2}{c_S^2}\right)^3 - 8\left(\frac{c_R^2}{c_S^2}\right)^2 + 8\left(3 - \frac{2}{\gamma^2}\right)\left(\frac{c_R^2}{c_S^2}\right) - 16\left(1 - \frac{1}{\gamma^2}\right) = 0 \quad (3.13)$$

where $\gamma \equiv v_L/v_T$. In case that $0 < (\frac{c_R^2}{c_S^2}) < 1$, the velocity has physically meaningful value. According to Eq.3.13, the ratio $\frac{c_R}{c_S}$ is a function of the ratio of γ . たとえば、KAGRA と同じ山の下に建設された 100m の重力波望遠鏡 CLIO での P 波と S 波の位相速度はそれぞれ AA、BB である [?] ので、 $\gamma = 1.82$ である。したがってこのときのレイリー波の位相速度は CC である。

3.1.2 Reduction Effect in the Deep Sites

レイリー波の振幅は深さに依存しており、深いほど小さくなる。

3.1.3 Reduction Effect of the Short Baseline

For interferometric gravitational-wave detectors which need a precise length control of the optical resonate cavity, it is appropriate to consider about the relative displacement between two points rather than the displacement of single point.

Differential Motion and Common Motion

We define the motion of two points shown in Fig.(3.1) as $\mathbf{u}_1 = \mathbf{u}(t, \mathbf{x}_1)$ and $\mathbf{u}_2 = \mathbf{u}(t, \mathbf{x}_2)$, respectively. The motions of the two points can be represented as the differential motion and the common motion. The displacement of both differential motion and common motion of the two points shown in Fig.(3.1) are defined as

$$\mathbf{u}_{\text{diff}} \equiv \frac{\mathbf{u}_1 - \mathbf{u}_2}{\sqrt{2}}, \quad (3.14)$$

$$\mathbf{u}_{\text{comm}} \equiv \frac{\mathbf{u}_1 + \mathbf{u}_2}{\sqrt{2}} \quad (3.15)$$

These two motions defined in Eq.(3.14) and Eq.(3.15) are normalized by $\sqrt{2}$ to conserve the total power.

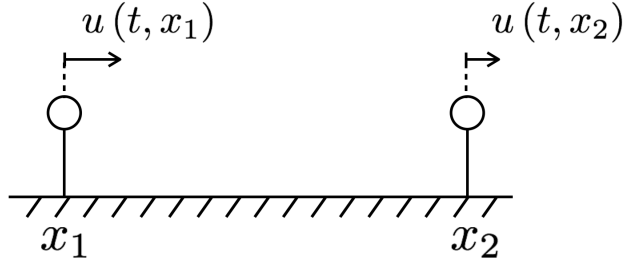


Figure 3.1: The displacements of the two points which are separated L in X axis. $\mathbf{u}(t, \mathbf{x})$ is the displacement field vector, where t denotes the time and \mathbf{x} denotes the location vector.

Common and Differential Motion Ratio (CDMR)

We define the power ratio of the common motion over the differential motion as common and differential motion ratio (CDMR). This ratio is useful to describe how the differential motion is reduced in the baseline compared to the common motion. CDMR is defined as

$$\text{CDMR} \equiv \sqrt{\frac{\text{Common Motion}}{\text{Differential Motion}}} = \sqrt{\frac{P_{\text{comm}}(\omega)}{P_{\text{diff}}(\omega)}} \quad (3.16)$$

where $P_{\text{comm}}, P_{\text{diff}}$ are the power spectral densities (PSDs) of the differential motion and common motion, respectively. In order to obtain these PSDs, we convert from the autocorrelation function of these. Therefore, first, autocorrelation function C_{diff} of the differential motion is given by its definition in Eq.(3.15)

$$C_{\text{diff}}(\tau) = \frac{1}{2} \left\langle \left[x_1(t) - x_2(t) \right] \left[x_1(t + \tau) - x_2(t + \tau) \right] \right\rangle \quad (3.17)$$

$$= \frac{1}{2} \left[C_{11}(\tau) - C_{12}(\tau) - C_{21}(\tau) + C_{22}(\tau) \right], \quad (3.18)$$

,where C_{ij} are the autocorrelation functions of each point and defined as $C_{ij} \equiv \langle x_i(t)x_j(t + \tau) \rangle$, ($i = 1, 2, j = 1, 2$). Here, one can obtain the power spectrum density of differential motion $P_{\text{diff}}(\omega)$ as

$$P_{\text{diff}}(\omega) = \frac{1}{2} \left[P_1(\omega) + P_2(\omega) - P_{12}(\omega) - P_{12}^*(\omega) \right] \quad (3.19)$$

$$= \frac{1}{2} \left[P_1 + P_2 - \text{Re}[\gamma] \times 2\sqrt{P_1 P_2} \right], \quad (3.20)$$

where $P_1(\omega), P_2(\omega)$ are the power spectrum densities of each points, and $P_{12}(\omega)$ are the cross spectrum between two point. The parameter γ is the complex coherence between them defined by

$$\gamma \equiv \frac{P_{12}}{\sqrt{P_1 P_2}}. \quad (3.21)$$

Furthermore, assuming that seismic wave propagating each points does not decay, which means $P_1 = P_2 \equiv P$, one can compute the $P_{\text{diff}}(\omega)$ as

$$P_{\text{diff}}(\omega) = P(1 - \text{Re}[\gamma]). \quad (3.22)$$

Similarly, the PSD of the common motion can be calculated as

$$P_{\text{comm}}(\omega) = P(1 + \text{Re}[\gamma]). \quad (3.23)$$

Finally, CDMR defined Eq.(3.16) in case the seismic wave does not decay is represented as

$$\text{CDMR} = \sqrt{\frac{1 + \text{Re}[\gamma]}{1 - \text{Re}[\gamma]}}. \quad (3.24)$$

Eq.(3.24) indicates that CDMR can be expressed by only the coherence γ between of two points. For example, CDMR tends to be larger when γ close to 1. This means that the differential motion is more less than the common motion because the two points move together in the same direction.

Uniform Plane Wave Model

Consider the CDMR when the plane waves are distributed uniformly around the azimuth. Because the coherence that the single plane wave propagating with the azimuth angle θ along the direction of arm cavity from x_1 to x_2 in Fig.(3.1) is

$$\gamma = e^{i \frac{L \cos \theta \omega}{c}}, \quad (3.25)$$

the coherence in case that the plane waves propagats uniformly is given by the integral of Eq.(3.25) over all direction;

$$\gamma = \frac{1}{2\pi} \int_{-\pi}^{\pi} e^{i \frac{\omega}{c} L \cos \theta} d\theta. \quad (3.26)$$

where the coherence is normized azimuth angle. Therefore, the CDMR is given as

$$\text{CDMR} = \sqrt{\frac{1 + J_0\left(\frac{L\omega}{c}\right)}{1 - J_0\left(\frac{L\omega}{c}\right)}}. \quad (3.27)$$

For later discussion in 3.3.5, the PSD of the differential motion in case of the uniform seismic waves is usefull and is given as

$$P_{\text{diff}}(\omega) = P \left[1 - J_0 \left(\frac{L\omega}{c} \right) \right]. \quad (3.28)$$

3.2 Seismic Noise

Here we describe the actual seismic noise. Characteristics of the seismic noise are related with its origin spatially and temporally. The noise sources are spreaded anywhere; foot steps, traffics and ocean waves, and these amplitude depends on day-night or weather condition.

As summarized in Table 3.2, the seismic noises above 1 Hz are cleary correlated with cultural activities, and that below this frequency are excited by the natural phenomena [?].

Table 3.1: Two types of seismic noise

Type of noise	Frequency Band	Sources
Cultural Noise	> 1 Hz	wind, traffic, machinaries, foot steps
Natural Noise	< 1 Hz	ocean, air pressure, earth tides

This boundary frequency between cultural or natural is depends on the soil structure. At the sediment site such as the LIGO[?] and Virgo site[?], the cultural noise can be shifted to a lower frequency and appear below 1 Hz. On the other hands, at the hard rock site such as KAGRA site, the cultural noise can be distinguished from the natural noise for its diurnal variability and apparent only above 1 Hz.

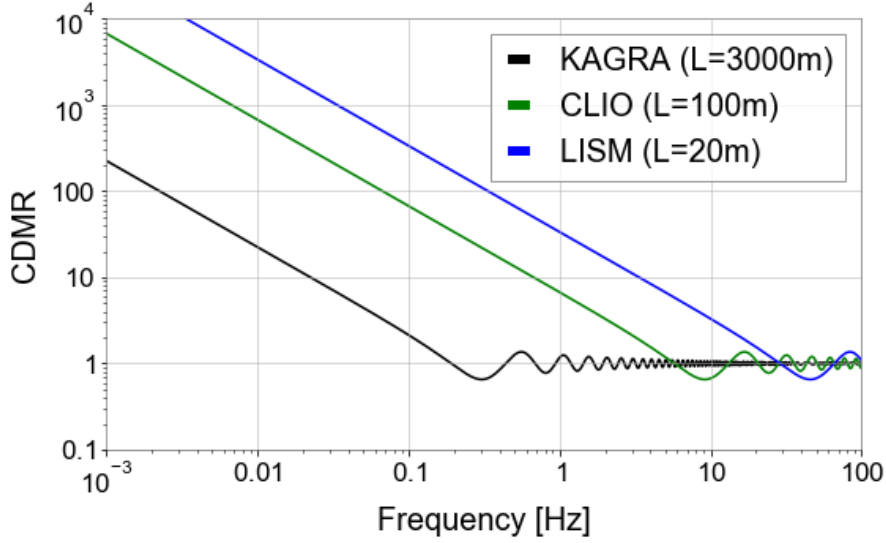


Figure 3.2: CDMR, which is the power ratio of the common motion over the differential motion of baseline in Eq.(3.27), of the underground GW detectors assuming the uniform plane waves model with phase velocity of 3000 m/sec. Black is KAGRA with the 3000 m baseline, green is CLIO with the 100 m baseline, and blue is LISM with the 20 m baseline. The CDMR of the long baseline is worse than that of short baseline. For example, at 0.1 Hz, if the baseline length is longer, the CDMR is larger..

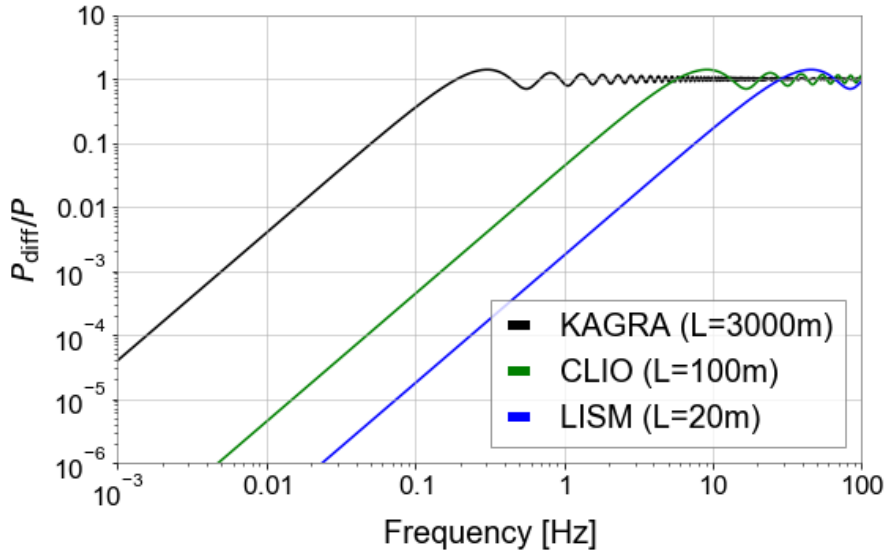


Figure 3.3: The power ratio of the differential motion of the baseline over the motion at single point; P_{diff}/P of Eq.(3.28). This ratio gives the estimation of the PSD of baseline length fluctuation from the

3.2.1 Cultural Noises

The cultural seismic noise contaminates the sensitivity of gravitational-wave detectors in the frequency range of interest for gravitational-waves sources, above 1 Hz. In this frequency band, the cultural noise is dominated by winds or human activities. For example, seismic noise from traffic near the detectors is reported at LIGO site [?], and noise from the vibrations of building excited by winds is reported at Virgo site [?].

3.2.2 Natural Noises

The natural seismic noise affects the stability of the GW detectors below 1 Hz because it deforms largely the ground on which mounted the detectors.

これら natural seismic noise は場所によって大きく異なることが知られている。Peterson らによって行われた、世界の 75 箇所の基地にある地震計の数年分のデータから得た地面振動のノイズスペクトルを Figure 3.4 に黒線で示す。200 mHz のピークは

Microseisms

Microseisms which power spectrum has peaks in 50–200 mHz are excited by oceanic waves. These seismic waves can be categorized by the generating mechanism of these [?]. First, the primary ocean microseisms are generated only in shallow waters in coastal regions. In this regions, the water wave energy can be converted directly into seismic energy either through vertical water pressure variations, or by the impacts of surf on the shores. There are correlation between this microseismic peak and the swell at the beaches was known starting from the data sets studied by [?]. Second, the secondary ocean microseisms could be explained by the superposition of ocean waves of equal period traveling in opposite directions. Therefore, generating standing gravity waves of half the period [?].

The RMS amplitude spectral of both type of the microseisms are strongly depends on the low pressure on the ocean [?].

Seismic Noise Below 20 mHz

Below the microseismic frequency band, the main seismic noise source is an atmospheric pressure change; Rayleigh waves excited by air fluctuation on the surface, and the deformation of the Earth's crust caused by the Newtonian attraction of air mass fluctuation [?, ?]. Fig. 3.5 shows PSDs of the New Low Noise Model (NLNM) [?] and the measured former noise [?], and the noise is consistent with the NLNM between 2 Hz and 30 mHz. Moreover, the latter noise is increase PSD increases rapidly with decreasing frequency below 2 mHz. ここで特筆すべきは、2mHz 以上のノイズは Rayleigh wave で運ばれるため、地下に

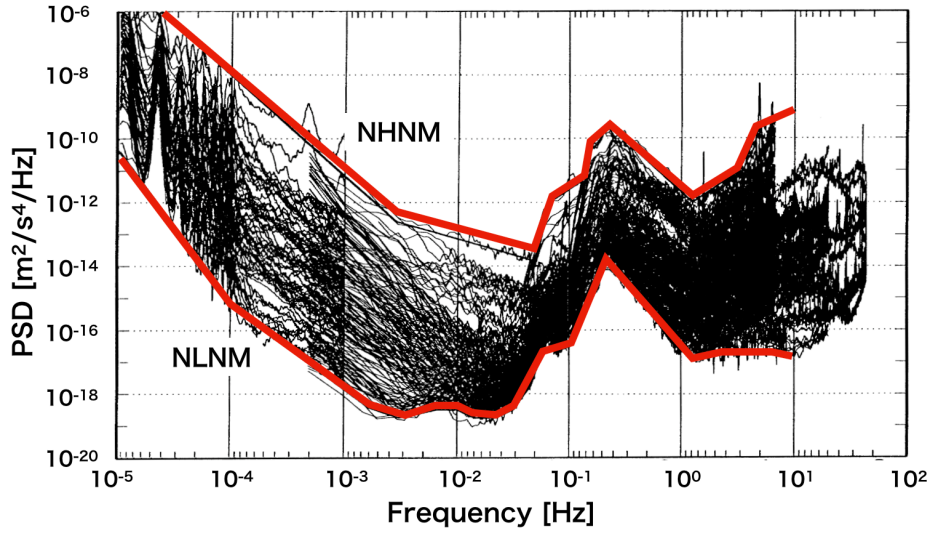


Figure 3.4: PSDs of the seismic noise obtained by Peterson in 75 stations in the world [?]. Each of the black solid lines is PSD divided into 5 different frequency band at the each stations. Each red lines are the new high noise model (NHNM) and the new low noise model (NLNM), respectively. The NHNM a spectrum of average high background noise power in the seismometer network, and the primary contributions to NHNM are inland stations situated on soft solid in very noisy locations and coastal stations with high amplitude microseisms. The NLNM represents the seismic noise when microseismic is quiet, and below microseismic, it represents the global seismic noise floor[?].

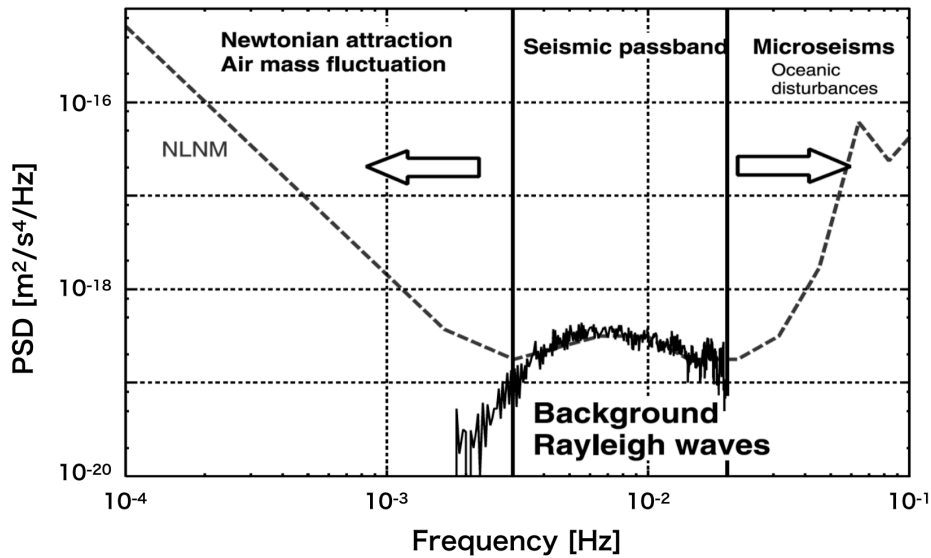


Figure 3.5: [?] から転載。

潜ればいくらか低減が期待されることである。実際に地表と地下のひずみ計による観測によってそれが示唆されている [?].

Earth tides

Below more lower frequency, the earth deformed by tidal forces due to the attraction of the Sun and the Moon in diurnal and semi-diurnal period.

(なにかもう少し書く)

3.3 Study of Seismic Noise of KAGRA Mine

3.3.1 Overview

KAGRA では、我々は地面振動を地震計とひずみ計をつかったリアルタイムモニターシステムを構築している。このシステムの目的は、地面振動に最も敏感な腕共振器を懸架する TypeA サスペンションの地面振動をモニターすることである。そのため、我々は広帯域地震計である Trillium120 を 3 台、TypeA が懸架されているコーナーエリアと両エンドエリアの二階の地面に設置し、ひずみ計は現在 X アームに設置している。これらセンサーは自身のセンサーノイズの特性上、帯域を相補的に地面振動をモニターしている；0.1Hz 以上は地震計で、1Hz 以下はひずみ計でモニターしている。

本節ではこれらセンサーをつかって、KAGRA の地面振動ノイズの時間的空間的な特徴を調べた。

3.3.2 Experimental Arrangement

We used Trillium 120-QA which is known as three-component, very broadband, and low-noise seismometer. These three outputs are proportional to the ground velocity of two horizontal and one vertical, respectively.

The seismometer is housed in the black thermal insulation cover as shown in fig 3.6. Thermal insulation protects two broad categories of thermal couplings that can cause unwanted noise [?]. First is the direct coupling to the sensitivity. This coupling typically increases the noise of the vertical channel as a periodic diurnal variation caused by the day-to-night temperature cycle, because the springs that suspended the inertial masses are temperature sensitive. The second is the coupling to tilt from the thermal fluctuation. Tilt converts the vertical acceleration of gravity into horizontal acceleration. This thermally induced tilt noise on the horizontal will be larger than the direct thermal coupling on the vertical channel. To be low sensitivity to both tilt and temperature, this model has a function to center the inertial mass after the initial installation.

The signals of the seismometer is recorded through the data aquisition system developed by LIGO [?]. The analog signal is converted to digital signal by the 16 bit analog-to-digital converters (ADC) with 16384 Hz sampling. This



Figure 3.6: Trillium 120-QA installed on the second floor at X-end area, which is covered by black thermal insulation cover

analog signal is amplified with 30 db so that the ADC noise does not mask this signal.

3.3.3 Data Processing

振幅スペクトルの推定は 50%オーバーラップした 32 個のセグメントの平均で得た。それぞれのセグメントの FFT の計算は、まず dtrend をして線形成分を取り除き、Hanning 窓にかけてから行った。32 回の平均をおこなったスペクトルは自由度 32 のカイ二乗分布に従う。自由度 ν のときの $100(1-\alpha)\%$ の信頼区間は、周波数 f でのスペクトルの推定量を $\hat{G}(f)$ とすると、

$$\frac{\nu \hat{G}(f)}{\chi^2(\nu, 1 - \frac{\alpha}{2})} \leq G(f) \leq \frac{\nu \hat{G}(f)}{\chi^2(\nu, \frac{\alpha}{2})} \quad (3.29)$$

で与えられる。したがって、95%の信頼区間は

$$\nu / \chi^2(\nu, 1 - \frac{\alpha}{2}) \leq G(f) / \hat{G}(f) \leq \nu / \chi^2(\nu, \frac{\alpha}{2}) \quad (3.30)$$

となり、自由度 32 の場合、推定量の 0.65 から 1.75 の範囲になる。

3.3.4 Study of Long-term Seismic Noise

Long-term seismic noise is measured by a seismometer installed on the second floor of the X-end area. This area is placed 200 m underground from the surface of the mountain. In comparison to corner area, human activity in the end area is less because the corner area has parking lots. In comparison to the Y-end area, there is no entrance connected to other mines. Therefore, the X-end area is relatively quiet in the KAGRA mine, regarding the seismic noise induced by human activity.

地震や回路からの突発的なノイズを含まない一年間のデータをつかって、ノイズスペクトルを計算した。並進成分と垂直成分両方の加速度の ASD を Figure 3.7 に示す。40mHz 以上では並進成分も垂直成分も同じ振幅スペクトル密度をもつ。40mHz 以下で並進成分が垂直成分よりも大きい、これは付録で後述しているとおろ、無相関なノイズである。おそらく温度ゆらぎから生じる傾斜カップリングだと考えられる。また、Peterson のスペクトルと測定で得た 10 パーセンタイルを比較すると、0.1 から 2Hz をのぞいて、NLNM と同じである。0.1Hz 以下では垂直成分は地面振動のノイズレベルと同等であり。2Hz 以上は、並進も垂直成分も、地下環境のおかげで静かである。対照的に 0.1 から 2Hz の帯域では、並進成分も垂直成分も NLNM より数倍大きい。これは KAGRA が富山湾から 40km の距離にあり、比較的脈動の影響を受けやすいためと考えられる。

3.3.5 Study of the Differential Motion Reduction

CDMR in X-arm

3.1.3 で述べた CDMR の効果を、X アームの両端においた地震計 2 台をつかって評価した。

基線長の違いによる CDMR の変化

aaa

3.4 Summary of the Chapter

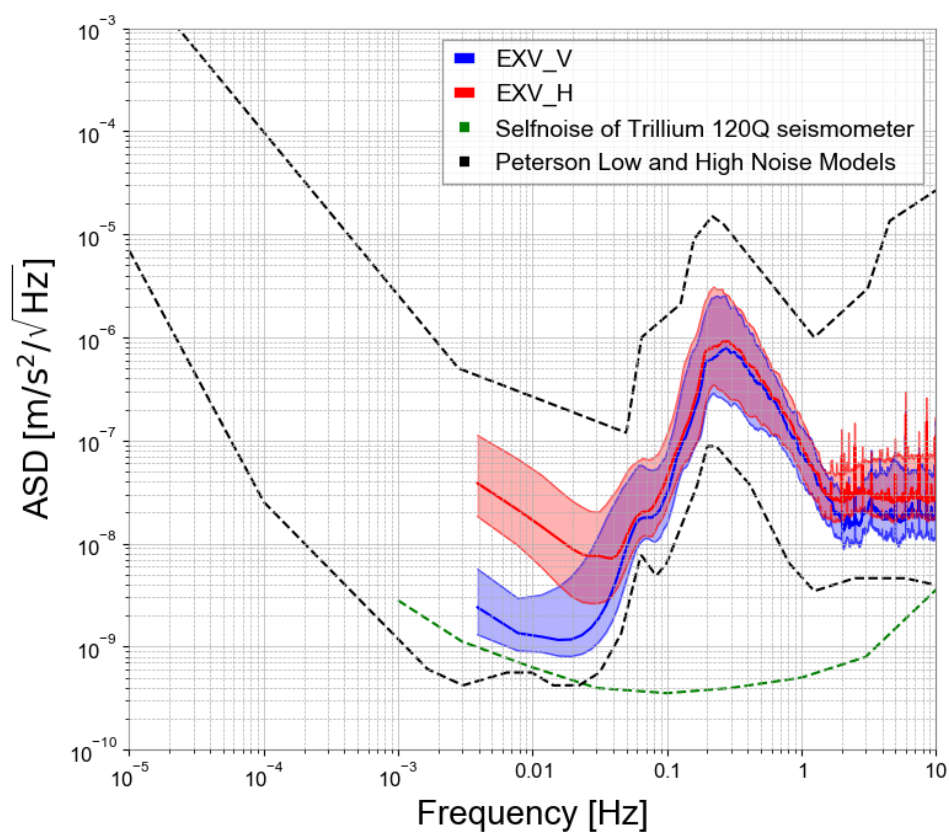


Figure 3.7: 赤の実線は垂直成分の 50 パーセンタイルで、下と上に 10 と 90 パーセンタイルを示す。青の実線は X 軸と Y 軸の二乗和から求めた並進成分であり、同様に 10,50,90 パーセンタイルを示す。緑点線は Trillium120 のデータシートから引用した Selfnoise である。黒の点線は Peterson の NLNM と NHNM である。

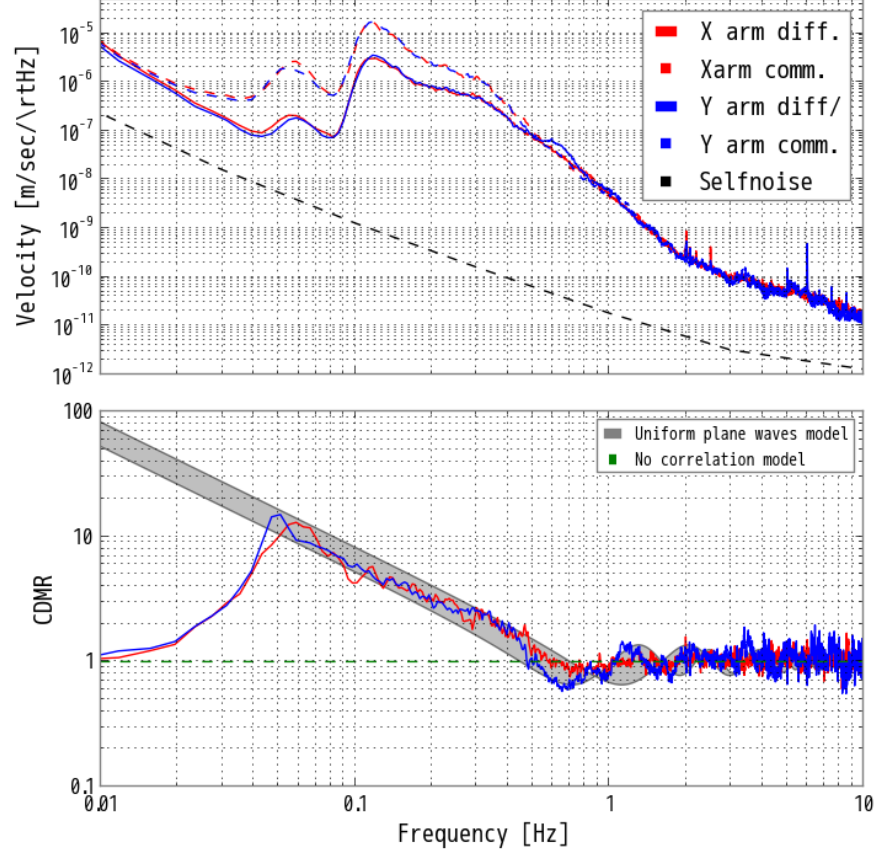
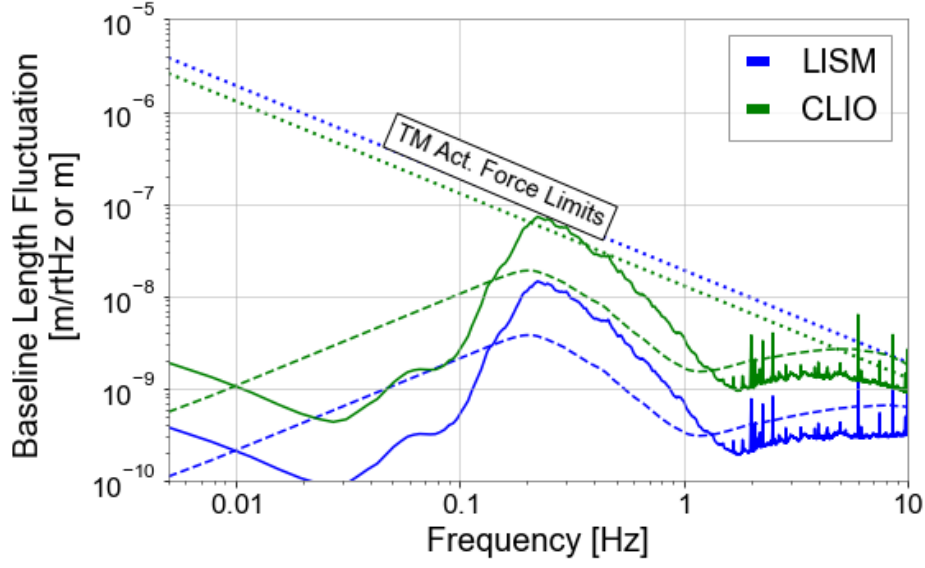
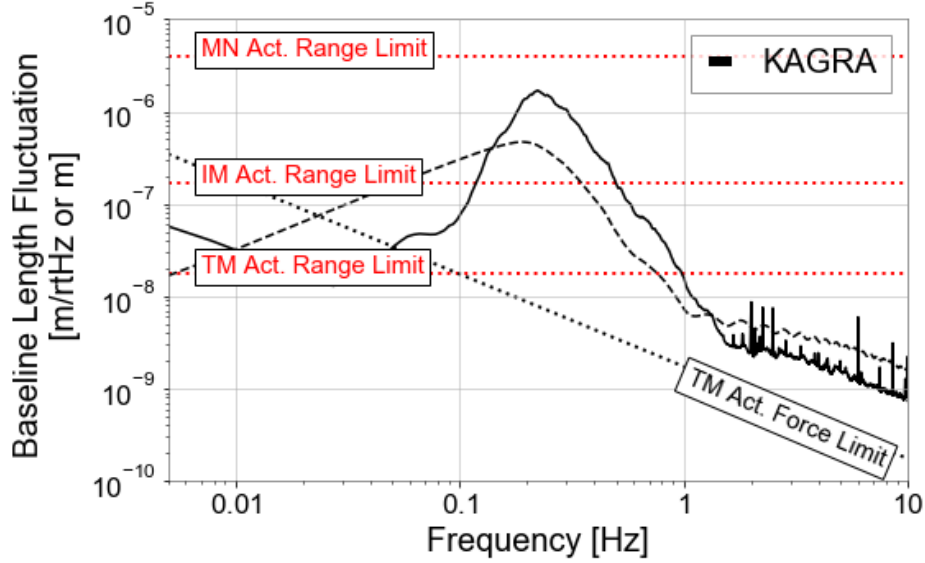


Figure 3.8: Comparison with the measured CDMR and the uniform plane waves model. (Top) ASDs of the velocity of the differential (solid line) and common motion (dashed line) of the baseline used calculating the below CDMR. Red and blue indicate X-arm and Y-arm, respectively. As a comparison to these ASDs, black dashed line shows the selfnoise of the Trillium 120Q broadband seismometer multiplied $\sqrt{2}$. Below 0.05 Hz, the ASDs are limited by the noise mentioned in section 3.3.2. (Bottom) The CDMR of the baseline calculated with the differential and common motion of the baseline according to the definition in Eq.(3.16). Gray line indicates the CDMR assuming the uniform plane waves model in case the phase velocity is in region from 5 – 3 km/sec. Green dashed line is the CDMR assuming the no correlation between the each end points of the baseline. The measured CDMR is consistent with the uniform model in 0.05 – 0.5 Hz. Below this band, the CDMR is close to the no correlation model due to the noise of the seismometers. Above this band,



(a)



(b) Comparison between the baseline length fluctuations and the displacement requirement of the underground GW detectors. Solid line is the baseline length fluctuation of the detectors, which is the ASD of the seismic noise (described in section 3.3) multiplied by the function in Eq. ?? assuming the uniform plane wave model with the phase velocity of 3 km/sec. Moreover, dashed line is the accumulated RMS of the fluctuations. As a comparison, the displacement requirement of the detector, which is the linewidth of the arm cavity, is plotted.

Figure 3.9: aa

Table 3.2: Comparison of the underground GW detectors

Detector	Baseline length [m]	Linewidth [μm]
LISM	20	0.1
CLIO	100	0.1
KAGRA	3000	0.1

Chapter 4

Geophysics Interferometer (GIF)

4.1 Introduction

地物干渉計の目的は、地球物理学の現象を精密に測定することと、KAGRA の基線長をモニターすることである。

4.1.1 Laser Strainmeter for Geophysics

4.1.2 Motivation in GW detectors

4.2 Working Principle

4.2.1 Asymmetric Michelson Interferometer

$$\phi = 2\pi \frac{2(l_x - l_y)}{\lambda} \sim 4\pi \frac{l_x}{\lambda} \quad (4.1)$$

$$|d\phi| = 4\pi \frac{l_x}{\lambda} \left(\left| \frac{d\lambda}{\lambda} \right| + \left| \frac{dl_x}{l_x} \right| \right) \quad (4.2)$$

4.2.2 Response to the seismic strain

The response of the strainmeter to seismic waves have characteristics of the low pass filter. To calculate this response, it is assumed that the plane seismic waves which displacement $u(x, t)$ is represented as $u(x, t) = u_0 e^{i(\omega t - kx)}$ with angular frequency of ω and wave number of k , propagate along with the direction of the base-line of the strainmeter. The length fluctuation between two mirrors

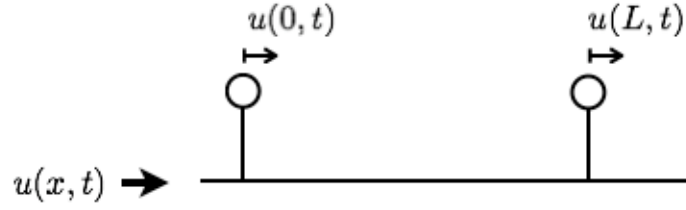


Figure 4.1: The displacements of the two points which are separated L in X axis.

separated with L can be expressed as

$$\Delta L(t) \equiv u(0, t) - u(L, t) \quad (4.3)$$

$$= u(0, t) - u(0, t - \tau), \quad (4.4)$$

where $\tau = L/v$ is the time delay. The transfer function from the displacement to the length fluctuation is

$$H_{\text{disp}}(s) \equiv \frac{\Delta L(s)}{u(s)} = 1 - \exp(-\tau s) \quad (4.5)$$

Because the strain amplitude $\epsilon(x, t)$ is defined as $\epsilon(x, t) \equiv \frac{du}{dx}$, the strain

$$\epsilon(x, t) \equiv \frac{du}{dx} = \frac{du}{dt} \frac{dt}{dx} \quad (4.6)$$

$$= u(x, t)' \frac{1}{v} \quad (4.7)$$

Therefore, the response of the strainmeter to the seismic strain is given

$$H_{\text{strain}}(s) \equiv \frac{\Delta L(s)}{\epsilon(s)} = \frac{\Delta L(s)}{\frac{s}{v}u(s)} = (1 - \exp(-\tau s)) \frac{v}{s} \quad (4.8)$$

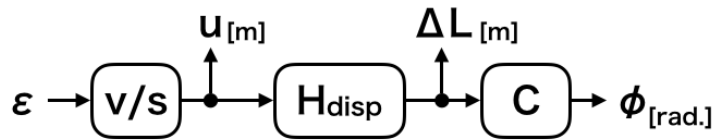


Figure 4.2

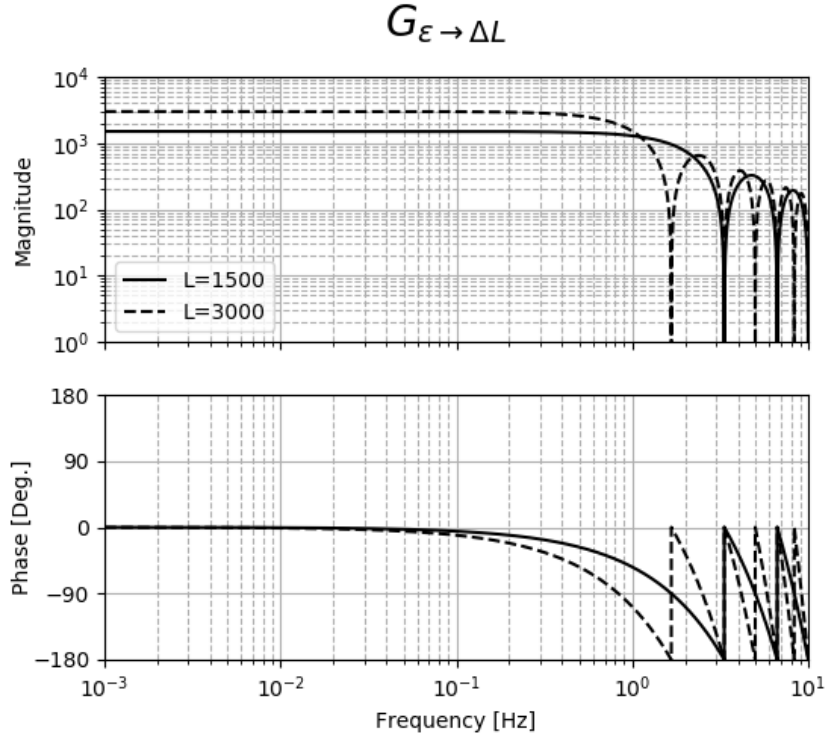


Figure 4.3: Transferfunction from strain of the baseline (ϵ) to the length change of that (ΔL).

4.2.3 Signal Detection Scheme

Quadrature Phase Detection

4.2.4 Noise

どういふノイズが原理的に存在するか述べる。空気ゆらぎ、周波数雑音を述べる。

4.3 Optics Design

...

4.3.1 Overview

Optical layout is shown in Fig. ???. Optics of GIF is categorized by three category; mode-matching optics, core optics and frequency stabilized laser.



Figure 4.4

4.3.2 Design Concept

設計で考慮しなければならない点は*干渉位置で2つのモードが合っていること
*できるだけ光学系は小さくすることである。

腕の長さから生じるモードのズレを小さくするために、エンドリフレクタで
ビームウエストを持つようにする。

4.3.3 Input Output Optics

4.3.4 Core Optics

4.3.5 Frequency Stabilized Laser

4.4 Data Acquisition System

4.4.1 Realtime Processing

4.4.2 ...

4.5 Summary of the Chapter

本章で述べたパラメータを表にまとめる。

Chapter 5

Arm Length Compensation System for Global Seismic Control

5.1 Introduction

Seismic noise cause two main problems to the terrestrial gravitational-wave detectors. First one is the limitation of the sensitivity. Amplitude spectrum density of the seismic noise, is empirically known as

$$\sim \frac{10^{-7}}{f^2} \text{ m}/\sqrt{\text{Hz}}, \quad (5.1)$$

where f is a frequency of the spectrum. This noise limits the sensitivity of the detectors in lower frequency typically below 10 Hz even after the attenuation by the vibration isolation systems. On the other hands, second problem is the decrease of the duty cycle of the GW detectors. Laser interferometric detector has an Fabry-Perot optical resonant cavities to enhance the sensitivity of GWs. This optical cavity only resonant within the narrow linewidth of few nm, whereas the seismic noise is larger than this width by two orders of magnitudes.

Underground can resolve these problems. Underground is more quiet than the surface of the ground [?]. Especially, the underground seismic noise above 1 Hz is effectively reduced than the noise on surface of the ground [?]. For example, a laser interferometer gravitational wave antenna with a baseline length of 20 m (LISM) constructed underground have demonstrated the stable performance of the detector by resulting the high duty cycle of 99.8 % [?].

しかし、KAGRA のような 3km の長期線のレーザー干渉計では、LISM のように安定して可動させることは難しいとされている。なぜならば、地面振動による基線長変動は、基線長が長いほどその影響は大きいためである。後述する 3.3 に

よれば、0.2Hz の脈動による基線長変動への影響は、KAGRA は LISM の 150 倍ある一方で、表??に示すように、線幅はおよそ 17 倍しかない。つまり KAGRA は LISM と比べて、線幅に対して地面振動による基線長伸縮はおよそ 1 桁大きいことを意味する。このような長期線化による問題は、KAGRA などの第二世代の検出器だけの問題ではなく、ET などの数 10km の基線長を計画する第 3 世代の検出器にとって同様の問題となる。

Table 5.1: Comparison of the line width of the arm cavity

	Finess	Line width [μm]	Baseline length [m]
LISM	25000	0.021	20
KAGRA	1500	0.35	3000

5.2 Basics in Vibration Isolation and Control Technique

5.2.1 Passive Vibration Isolation

Single Pendulum

Multi Pendulum

5.2.2 Active Vibration Isolation

5.2.3 Sensor Based Control Technique

5.2.4 2 Types Feedforward Control Techniques

Feedforward at Feedback Point

Feedforward at Error Point

5.2.5 Toward the Global Seismic Control

Overview

Suspension Point Interferometer

5.3 Difficulties in the Global Seismic Control

5.3.1 Overview

5.3.2 Actuator Range Limit

5.3.3 ...

5.3.4 ...

5.4 Arm Length Compensation Using Geophysics Interferometer

5.4.1 Concept

5.4.2 Geophysics Interferometer for Sensing the Arm Length

5.4.3 Arm Length Compensation

5.4.4 Requirements

5.5 Summary of the Chapter

Chapter 6

Demonstration of Arm Length Compensation Control

6.1 Experimental Arrangement

6.1.1 ...

6.2 Results

6.2.1 ...

6.3 Discussion and Summary of the Chapter

6.3.1 Discussion

6.3.2 Summary

Chapter 7

Conculusion and Future Directions

7.1 Conclusion

7.2 Future Directions